nature communications

Article

https://doi.org/10.1038/s41467-026-70945-8

Negative CO_2 emissions for long-term mitigation of extremes in land hydrological cycle

Received: 12 December 2024

Accepted: 10 March 2026

Published online: 23 March 2026

Check for updates

Jongsoo Shin[1], Jong-Seong Kug[2] ✉, So-Won Park[2], Jonghun Kam[3], Soon-Il An[3,4], So-Eun Park[4], Hyoeun Oh[5,6], Sang-Wook Yeh[7], Sujong Jeong[8,9], Chang-Kyun Park[9] & Jin-Soo Kim[10]

Global warming has profound effects on the terrestrial hydrological cycle, leading to alterations in regional extreme weather patterns. While terrestrial precipitation responses under continued greenhouse gas emissions are well established, the responses of terrestrial precipitation and vegetation feedbacks under climate mitigation scenarios remain uncertain. Here, we investigate terrestrial precipitation changes under idealized negative and zero CO_2 emissions scenarios using the Community Earth System Model version 2 (CESM2). Terrestrial precipitation increases by approximately 1.1% at the peak CO_2 concentration (~725 ppm), but shows even greater increases of about 1.9% and 2.5% under substantially lower atmospheric CO_2 concentrations following zero (~600 ppm) and negative (~430 ppm) CO_2 emissions, respectively. Our results suggest that enhanced transpiration from terrestrial vegetation largely contributes to this increase under the negative emissions scenario. Furthermore, despite a substantial increase in terrestrial precipitation, extreme precipitation events and droughts become less severe globally under the negative emissions scenario, even compared to the zero emissions scenario. While near-term mitigation is essential to curb immediate warming, these findings suggest that sustained negative emissions could be effective for achieving long-term reductions in hydrological extremes and enhancing terrestrial water availability.

Anthropogenic activities have led to a notable increase in carbon dioxide (CO_2) emissions[1]. The Paris Agreement aims to mitigate global warming by reducing emissions to achieve net-zero; however, increased temperatures are still anticipated[2,3]. Furthermore, to minimize the damage from future climate changes, it is necessary to reduce CO_2 concentrations through negative carbon emissions[4], along with considering large-scale climate intervention methods, such as climate engineering or geoengineering[5]. Despite these efforts, the climate system may not be able to return to its current state even if CO_2 levels are restored to current levels, meaning that the climate system is potentially irreversible[6–10].

[1]Physical Oceanography Department, Woods Hole Oceanographic Institution, Woods Hole, MA, USA. [2]School of Earth and Environmental Sciences, Seoul National University, Seoul, Republic of Korea. [3]Division of Environmental Science and Engineering, Pohang University of Science and Technology (POSTECH), Pohang, Republic of Korea. [4]Department of Atmospheric Sciences, Yonsei University, Seodaemun-gu, Seoul, Republic of Korea. [5]Center for Climate Physics, Institute for Basic Science, Busan, Republic of Korea. [6]Pusan National University, Busan, Republic of Korea. [7]Department of Climate and Energy Systems Engineering, Ewha Womans University, Seoul, Republic of Korea. [8]Department of Environmental Planning, Graduate School of Environmental Studies, Seoul National University, Seoul, Republic of Korea. [9]Climate Technology Center, Seoul National University, Seoul, Republic of Korea. [10]Department of Civil and Environmental Engineering, Korea Advanced Institute of Science and Technology, Daejeon, Republic of Korea. ✉e-mail: jskug@snu.ac.kr

So far, many studies have investigated the reversibility of the climate system, identified hysteresis behavior, and explored associated dynamical processes. These include the Atlantic Meridional Overturning Circulation (AMOC)[11–13], Intertropical Convergence Zone[14], monsoon[15,16], carbon uptake[17,18], vegetation[19], storm tracks[20], Hadley cell[21], drought area[18], extreme precipitation[22,23], global heat transport[24], global mean surface temperature[25–27], and regional precipitaion[25,27–29]. Among these climate systems, understanding the irreversible and hysteresis behavior of the hydrological cycle is particularly crucial for climate adaptation and mitigation policies, as its changes can have significant impacts on water availability, agriculture, and ecosystems. However, current knowledge of the hydrological cycles and associated extreme precipitation events that respond to increasing and decreasing CO_2 concentrations is still immature, so further research is needed to better quantify the impacts of climate change on the terrestrial hydrological cycle, water availability, and their extremes to inform effective policy decisions.

The plant physiological effect has climate feedback by altering the temperature and precipitation: For instance, the greening of the Earth due to CO_2 fertilization and global warming has caused the evaporative cooling effect due to increased leaf area[30]. However, under high CO_2 concentrations, the partial closure of plant stomata reduces plant transpiration, offsetting the fertilization effect in vegetation-rich areas[31–34]. This plant stomatal response causes surface warming[34–37] and significantly impacts the precipitation patterns[37,38] by changing the surface energy budget[39]. While this physiological effect can contribute to reduced precipitation in some regions, the rise in CO_2 levels increases near-surface temperature, thereby enhancing atmospheric moisture content by increasing the saturation water vapor pressure of air[40,41]. The combination of these feedbacks from the increased CO_2 emissions results in an overall increase in global precipitation. However, how plant physiological feedback plays a role in our climate system for the zero and negative CO_2 emissions remains uncertain. This study will show that the plant physiological effect enhances a future hysteresis behavior of the global land precipitation after the net-negative emissions.

To examine climate reversibility and hysteresis, we conducted two idealized CO_2 emission-driven experiments under the positive, negative, and zero emission scenarios with nine ensemble members ("Methods" and Supplementary Fig. 1). The first scenario, referred to as Z_E (zero emissions scenario), achieves zero emissions by the year 2125 by first increasing emissions linearly from the year 2001 to 2050 and subsequently decreasing them linearly to reach zero in 2124 (Supplementary Fig. 1a). The rate of increase until 2050 closely follows that of the Shared Socioeconomic Pathway 5-8.5 (SSP5-8.5) scenario. In this scenario, atmospheric CO_2 concentrations peak at 728 ppm in 2124, approximately 1.9 times the initial level of 383 ppm in 2000. The second scenario, referred to as N_E (negative emissions scenario), follows the same emission trajectory as Z_E until 2124 but then continues with negative emissions, reducing atmospheric CO_2 concentrations return to the present-day level of 383 ppm by 2197 (Supplementary Fig. 1b). Additionally, we performed a long-term integration experiment under zero CO_2 emissions until 2400 for both scenarios, extending for over 200 years, to determine whether climate system can revert to its current state, exploring climate reversibility. These experiments allow us to investigate the response of the global hydrological cycle under zero and negative emissions scenarios, as well as to evaluate the potential for reversibility of these changes.

Results

Land precipitation overshoot in the zero and negative emissions scenarios

Figure 1 illustrates the evolution of atmospheric CO_2 concentrations, mean surface air temperature (SAT), and precipitation changes in response to the CO_2 emissions scenarios, compared to the reference period (2001–2030). SAT increases over both ocean and land areas (excluding Antarctica) and then decreases in response to changes in CO_2 concentrations (Fig. 1a). SAT peaks at approximately 2.6 K over land and 2.0 K over ocean at the highest CO_2 concentration (728 ppm). After starting zero emissions in 2125 (Supplementary Fig. 1a), as the CO_2 concentration decreases slowly in Z_E (gray line in Fig. 1a), influenced by the carbon cycles among the atmosphere, ocean, and land[42].

The land SAT decreases slightly until 2250, while the ocean SAT remains stable during the same period (orange and sky-blue lines in Fig. 1a). Subsequently, SAT continuously increases until the end of the experiment, even as CO_2 concentrations decrease from roughly 728 to 600 ppm. In contrast, in N_E, SAT decreases as CO_2 concentrations reduce through the negative emissions until 2197 (red and blue lines in Fig. 1a). After CO_2 concentration returns to its initial level (383 ppm) (dark gray line in Fig. 1a), SAT increases until 2300, accompanied by 47 ppm increase in CO_2 concentration (i.e., 430 ppm) during this period. The rebound warming observed in Z_E and N_E can be attributed to the AMOC change[11,13,43], which is weakened by increased CO_2 concentrations but begins to gradually return to its initial state as the CO_2 levels decrease (Supplementary Fig. 2)[11,44]. Another contributing factor to the warming is the release of heat stored in the ocean, which effectively raises global temperatures, particularly in high-latitude regions[45].

Over the ocean, precipitation aligns with ocean SAT in both Z_E and N_E (sky-blue and blue lines in Fig. 1a, b), which relates to the warming-induced increase in water vapor supplied from the ocean. Similarly, land precipitation follows the trends of SAT but with differing amplitudes, particularly noticeable in N_E (red and orange lines in Fig. 1b). It is noted that the land precipitation in N_E (~2.6%) overshoots around 2300 compared to Z_E (~1.9%) and the peak CO_2 concentrations period (MAX, 2091–2120; ~1.1%), increasing by more than twofold. This land precipitation overshoot is particularly striking because the land and ocean SAT at that time is lower than those of Z_E and MAX (Fig. 1a). This indicates that while the increased land precipitation is tied to the delayed climate responses of the ocean[14,45]—where sustained warming

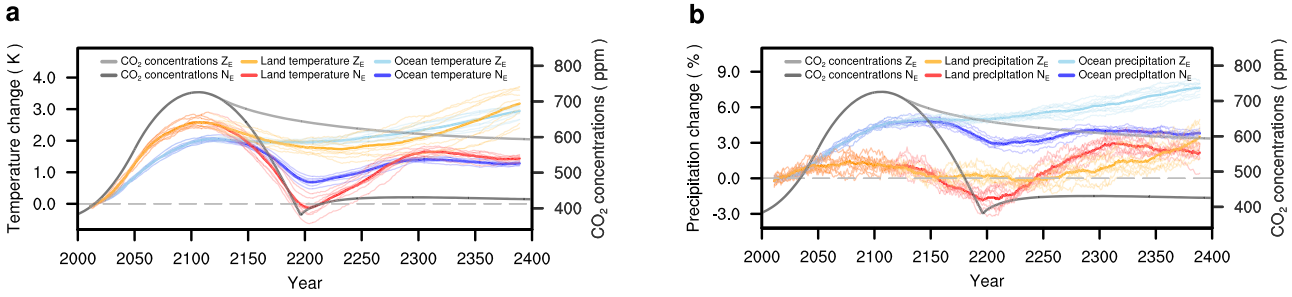


Fig. 1 | Evolution of the land and ocean temperature and precipitation under the zero emissions (Z_E) and the negative emissions (N_E) scenarios. a Time series of CO_2 concentration (dark gray for N_E, gray for Z_E), mean surface air temperature, and **b** precipitation over land (red for N_E, orange for Z_E) and ocean (blue for N_E, sky-blue for Z_E), respectively. Thick lines represent the ensemble mean, and thin lines are individual ensemble members. All variables are calculated as 21-year running means, relative to the reference period 2001–2030. Mean values are computed over the latitude range from 60° S to 90° N using land-sea masks.

https://doi.org/10.1038/s41467-026-70945-8

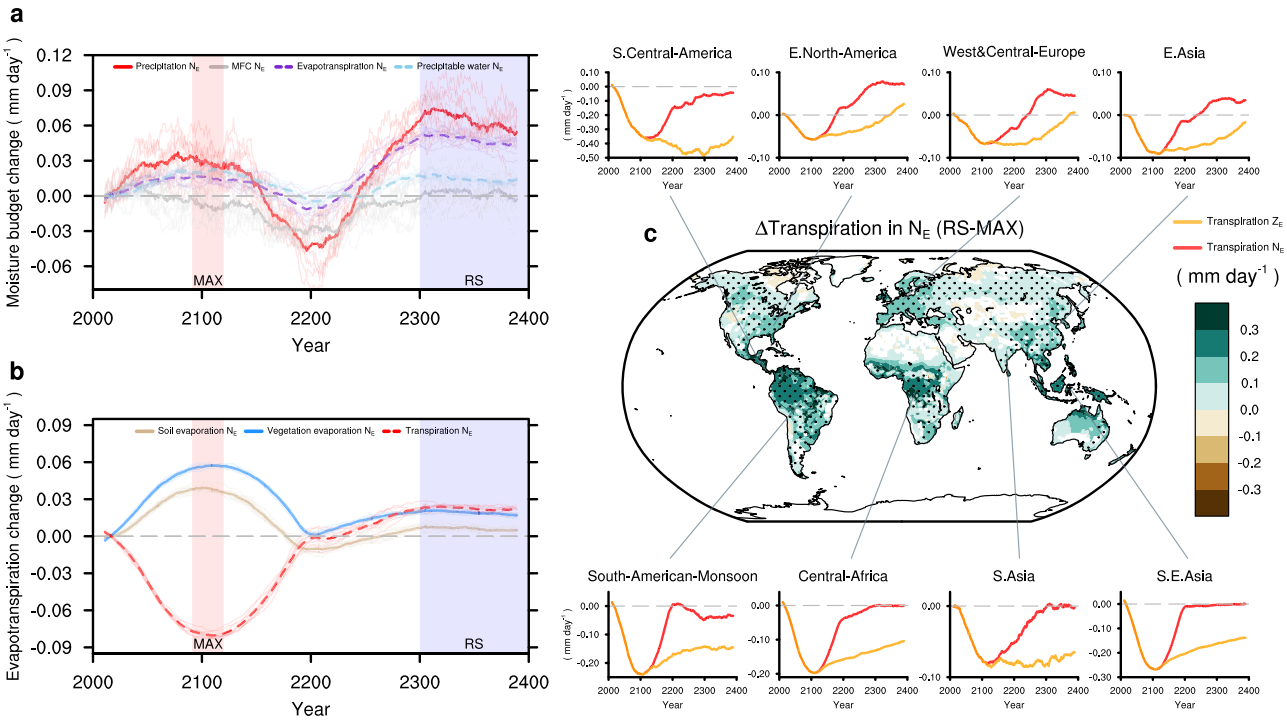


Fig. 2 | Changes in the global hydrological cycle. a Time series of mean land precipitation (red), moisture flux convergence (MFC, gray), evapotranspiration (purple dashed line), and the change in precipitable water (sky-blue dashed line) under the negative emissions (N_E) scenarios, relative to the reference period (2001–2030). **b** Time series of soil evaporation (beige), vegetation evaporation (blue), and transpiration (red dashed line) under N_E, respectively. Thick lines represent the ensemble mean, and thin lines indicate individual ensemble members. **c** Difference in ensemble mean transpiration between the restoring period (RS, 2300–2399, blue shaded in (a, b)) and the peak CO_2 concentration period (MAX, 2091–2120, red shaded in (a, b)) shown with mean transpiration time series over a specific region (see "Methods" section). The red line denotes N_E, and the orange line represents the zero emissions (Z_E) scenarios. Shading indicates that the change is statistically significant at the 95% confidence level. Areas where the annual mean LAI during the reference period exceeds 50% are marked with black dots. The Δ symbol indicates change. All the calculations are conducted after taking the ensemble mean and the 21-year running mean.

continues to drive atmospheric moisture changes—the magnitude of the overshoot cannot be solely attributed to an increase in water vapor content from air temperature increases. The increased land precipitation in N_E remains considerably high until the end of the experiment, resulting in similar amounts of land precipitation as in Z_E from 2300 to 2399 despite the considerable SAT difference (red and orange lines in Fig. 1b). These results suggest that not only the warming-induced water vapor from the ocean but also land-atmosphere coupled processes play significant roles in influencing land precipitation following the negative emissions.

Impact of physiological feedback on hydrological responses

To understand the land precipitation overshoot, we analyzed the land moisture budget, which includes precipitation, evapotranspiration, moisture flux convergence, and change in precipitable water (see "Methods" section). In N_E, transported moisture contributes little to the increase in precipitation during RS (gray line in Fig. 2a), while evapotranspiration rises considerably, suggesting a link to the increase in land precipitation during RS (red and purple lines in Fig. 2a). Evapotranspiration fluctuates in response to changes in CO_2 concentrations due to its dependence on temperature, affecting saturated humidity. Evapotranspiration shows symmetrical responses to increases and decreases in CO_2 concentrations during the positive and negative emission periods (purple line in Fig. 2a). However, from 2200 to 2399, the evapotranspiration in N_E displays a dramatic increase, accounting for approximately 75% of the changes in land precipitation during RS (red and purple lines in Fig. 2a). In Z_E, moisture flux convergence mostly shows negative values during the restoring period (RS, 2300–2399), indicating weakening of moisture transport from the adjacent oceans except towards the late 2300s (gray line in Supplementary Fig. 3a), contributing to a decrease in precipitation. Concurrently, evapotranspiration continuously rises when land precipitation rises (purple line in Supplementary Fig. 3a).

Evapotranspiration comprises water vapor fluxes from the ground (soil evaporation), wetted leaf and stem areas (evaporation of water intercepted by the canopy, also known as vegetation evaporation), and dry leaf surfaces via stomata (transpiration)[46]. We have analyzed these three components of evapotranspiration and found that their relative contributions vary significantly with CO_2 emissions (Fig. 2b and Supplementary Fig. 3b). Soil evaporation changes similarly to land precipitation but with weak variations (beige line in Fig. 2b). Vegetation evaporation exhibits patterns similar to land precipitation but with greater amplitude than soil evaporation (blue in Fig. 2b), associated with increased vegetation due to the CO_2 fertilization effect and global warming, known as the Greening Earth[30] (Supplementary Fig. 4). The change in transpiration, however, is the most dominant and closely follows the changes in CO_2 concentrations rather than land precipitation (Figs. 1b and 2b). In N_E, transpiration continuously increases after 2220 despite stabilized CO_2 concentration, contributing to increased land precipitation (red line in Fig. 2b). This indicates that the rise in evapotranspiration is largely driven by changes in vegetation, which combine vegetation evaporation and transpiration (Fig. 2b). Notably, the vegetation evaporation during RS in N_E is lower than during MAX, suggesting that the overshoot in land precipitation is closely associated with the transpiration. As the CO_2 concentrations rise, transpiration decreases due to stomatal closure (Supplementary Fig. 5). While the change in transpiration appears symmetrical to the CO_2 forcing, in N_E, it becomes the primary contributor to the increase in evapotranspiration (Fig. 2b). This underscores the critical role of transpiration in amplifying the overshoot of land precipitation.

https://doi.org/10.1038/s41467-026-70945-8

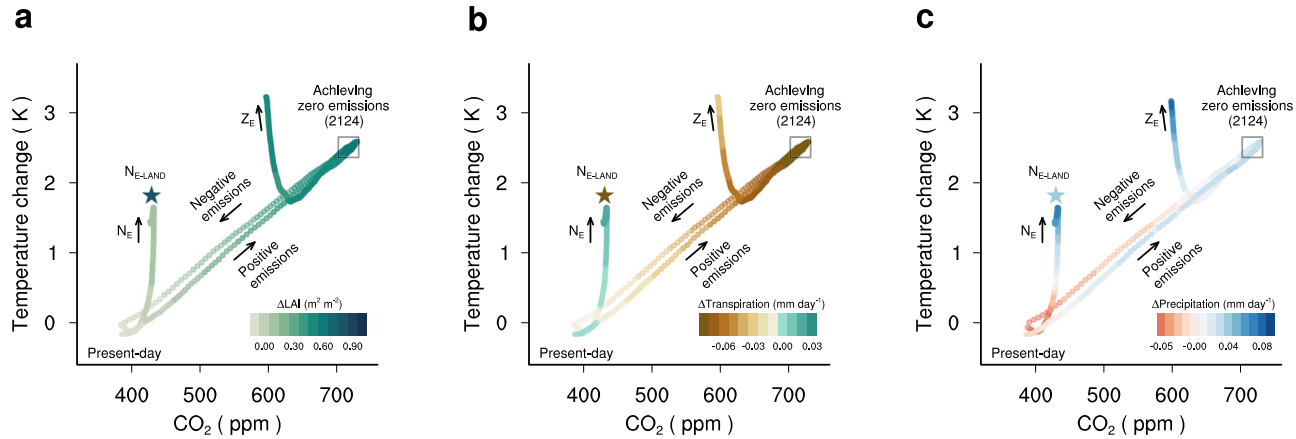


Fig. 3 | Response of temperature, LAI, transpiration, and precipitation to CO_2 concentration changes. Response of **a** global mean LAI, **b** transpiration, and **c** precipitation to CO_2 concentration and surface air temperature changes. The response illustrates the evolution of the climate system under positive, zero (Z_E), and negative emission (N_E) scenarios, relative to the reference period (Present-day, 2001–2030). The asterisk symbol represents the 100-year climatology from the $N_{E\text{-}LAND}$ experiment relative to the reference period. Arrows in each panel indicate the direction of CO_2 concentration changes over time. The square symbols denote the point in time when zero emissions are achieved in 2124. The Δ symbol indicates change. All data points represent the ensemble mean and are smoothed with a 21-year running mean.

Transpiration changes in N_E show an overall positive difference worldwide (Fig. 2c), particularly noticeable between RS and MAX (blue and red shadings in Fig. 2b). These changes are predominantly observed in densely vegetated areas, defined as regions where the leaf area index (LAI) exceeds 50% during the reference period (black dots in Fig. 2c). In the vegetation-rich regions such as South-Central America, South America, Central Africa, and Southeast Asia, transpiration significantly increases in RS compared to MAX. In both scenarios, the differences in transpiration during RS are substantial (red and orange lines in Fig. 2c). As CO_2 levels return to the present-day values, the associated transpiration changes contribute to increased precipitation, in contrast to MAX, when transpiration changes tended to offset precipitation increases (green shading in Fig. 2c). Furthermore, the pronounced increases in transpiration coupled with substantial rises in land precipitation are of sufficient magnitude to account for precipitation changes in certain regions (Fig. 2c and Supplementary Fig. 6a). This indicates the importance of land-atmosphere coupled processes in shaping precipitation patterns and highlights their role in the climatic response to changing CO_2 concentrations.

The increased transpiration in N_E is related to the physiological feedback of the terrestrial vegetation to CO_2 concentration changes. Transpiration is influenced by several factors, but total leaf area and stomatal closure are most important for response to changes in CO_2 concentration. Figure 3 shows responses of the land mean LAI, transpiration, and precipitation corresponding to the SAT and CO_2 concentration, which can help separate global warming and vegetation physiological effects. Under the positive emissions, as the CO_2 concentration and temperature rise, LAI also increases, possibly due to the combined impact of the fertilization and climate effects (Fig. 3a). Conversely, LAI decreases as the CO_2 concentration and temperature decline through the negative emissions. Interestingly, LAI in N_E continues to rise with warming despite a relatively constant CO_2 concentration (around 430 ppm), mainly observed in high latitude regions due to the increased temperature and precipitation during this period (Supplementary Fig. 7). In contrast, the change in LAI in Z_E is minimal due to the compensating effects between reduced CO_2 concentrations and increased temperatures (Supplementary Fig. 4). It is noted that LAI in Z_E still remains higher than in N_E, possibly due to higher CO_2 concentrations and warm conditions.

While LAI is positively correlated to the CO_2 concentration, transpiration decreases with increasing CO_2 concentration (Fig. 3b). This reduction is primarily due to the stomatal closure[47,48] (Supplementary Fig. 5). As atmospheric CO_2 levels rise, plants partially close their stomata to minimize water loss, thereby reducing transpiration[31,32,49,50]—an effect that often outweighs the CO_2 fertilization effect (i.e., increases in LAI) at higher CO_2 concentrations[33,34,37,51,52]. After achieving zero emission, transpiration in Z_E gradually recovers as CO_2 levels decrease, while transpiration in N_E becomes much stronger than that at its initial state due to higher temperature.

A concurrent rise in both land precipitation and transpiration is projected in N_E, marking a distinct departure from the positive emission phase, where transpiration decreased despite enhanced precipitation (Fig. 3b, c). This increase in transpiration further amplifies the precipitation response because transpiration is an important source for the precipitable water, accounting for approximately 53 to 60% of evapotranspiration in both observations and models[46]. In the meantime, more precipitation can lead to more transpiration through increased soil moisture, suggesting a two-way feedback. Additionally, the increase in LAI in N_E likely enhances transpiration, leading to more precipitation. With stable CO_2 concentrations, this additional precipitation provides the water necessary for vegetation growth, promoting more vegetation. In turn, this enhanced vegetation further increases water vapor supply through transpiration, creating a positive feedback loop that results in increased precipitation, even under low CO_2 concentrations and cooler ocean and land temperatures.

To further address the critical role of the stomata feedback in the land precipitation overshoot, an additional experiment ($N_{E\text{-}LAND}$) was conducted. In this experiment, the atmospheric CO_2 concentration was fixed at 430 ppm, corresponding to RS, while the CO_2 concentration influencing the vegetation module was set to 725 ppm, consistent with MAX (see "Methods" section). Therefore, only the vegetation experiences a higher CO_2 concentration, while the climate is influenced by the lower CO_2 concentration. When higher CO_2 concentrations are prescribed to the vegetation, land precipitation decreased, which is closer to the precipitation in MAX (Fig. 3c and Supplementary Table 1), representing only 35% of the increase seen in RS. Notably, transpiration decreases to levels similar to those during MAX (Fig. 3b). Although the increase in vegetation evaporation, associated with abundant vegetation, partially offsets the reduction in transpiration, total evapotranspiration declines compared to RS, contributing to the reduction in land precipitation (Supplementary Table 1). This experiment demonstrates that the reduction in transpiration due to the high CO_2 environment considerably contributes to the decrease in land precipitation, suggesting the critical role of the physiological feedback in the land precipitation overshoot.

https://doi.org/10.1038/s41467-026-70945-8

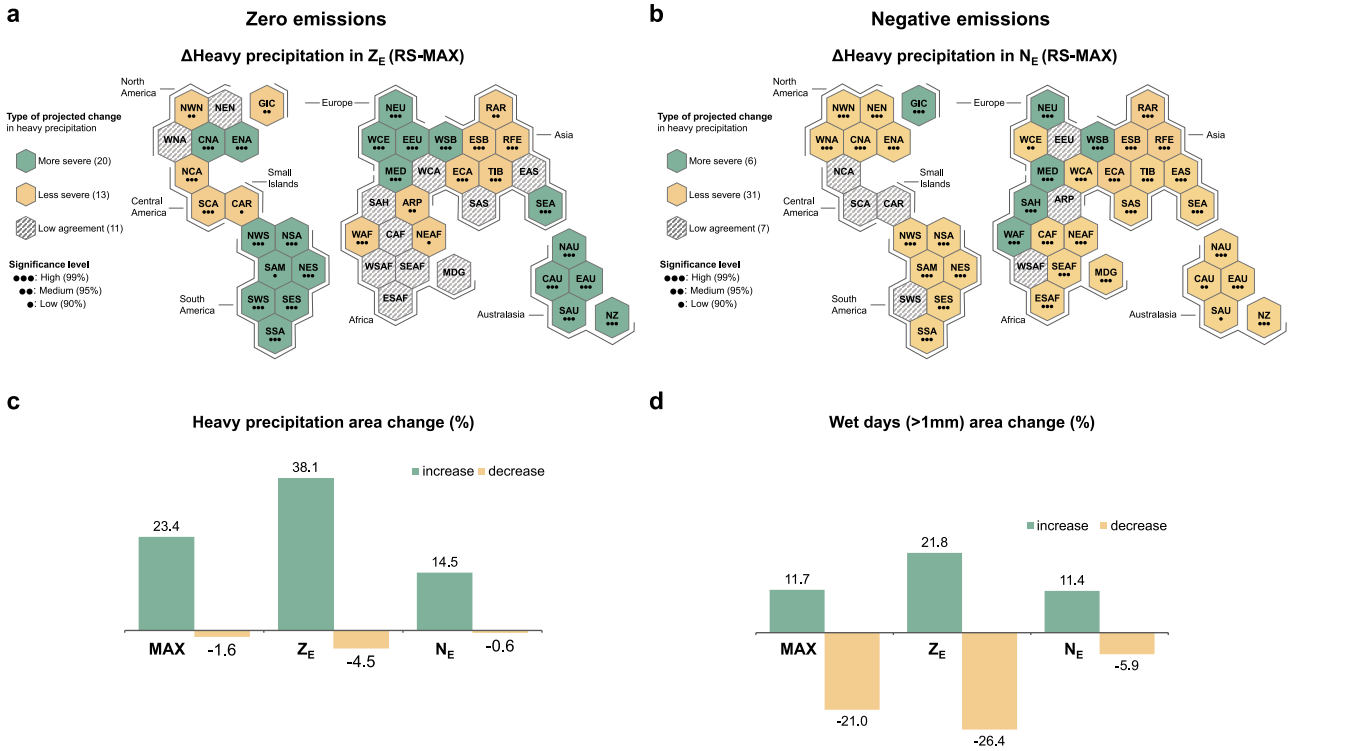


Fig. 4 | Synthesis of heavy precipitation attributable to regional changes. **a** Difference in heavy precipitation in the zero emissions scenario (Z_E) and **b** in the negative emissions scenario (N_E) between the restoring period (RS, 2300–2399) and the peak CO_2 concentration period (MAX, 2091–2120). Green hexagons indicate regions where there is at least low confidence in projected more severe events, and yellow hexagons indicate regions where there is at least low confidence in projected less severe events. Striped hexagons (gray) are insignificant for the type of change. The confidence level is indicated by the number of dots: three dots for high confidence (99%), two dots for medium confidence (95%), and one dot for low confidence (90%). The design and regional acronyms (see "Methods" section) used in (**a**, **b**) are reproduced with new data using Fig. 3 of the Summary for Policymakers (SPM) report[69]. **c** The changes in land fraction of heavy precipitation and **d** wet days for the MAX and RS periods in Z_E and N_E based on the reference period (2001–2030). These changes are statistically significant at the 95% confidence level.

Changes in extremes of the land hydrological cycle

Under global warming simulation, increased precipitation often tends to be directly linked to an increase in extreme precipitation events[53]. Concerns might arise that the augmented precipitation from the negative emissions could also exacerbate extreme precipitation events. To address this, we analyzed regional changes in the heavy precipitation/pluvial index, defined as the 1-day maximum precipitation (see "Methods" section), by comparing RS and MAX. In Z_E, regions including Eastern North America, South America, Europe, and Australia exhibit an increase in heavy precipitation alongside overall precipitation rises during RS compared to MAX (Fig. 4a and Supplementary Fig. 6a). In contrast, under N_E, most areas show a significant reduction in heavy precipitation (Fig. 4b). Despite the increase in precipitation compared to MAX, extreme events decrease in North South America, South American Monsoon, Western and Central Europe, and Southern East Asia regions (Supplementary Fig. 6a). Globally, the fraction of area, where heavy precipitation in the reference period is larger than 30 mm/day, affected by heavy precipitation increases by about 23.4% in MAX relative to the reference period, and this increase reaches 38.1% under Z_E (Fig. 4c). However, under N_E, it remains at 14.5% despite higher overall land precipitation levels. In other words, under the negative emissions, the overall increase in precipitation is not directly proportional to the increase in heavy precipitation; indeed, despite higher overall land precipitation increases, heavy precipitation events are relatively less severe.

Moreover, the negative emissions tend to alleviate the risk of near-surface soil moisture deficits (droughts). In Z_E, despite an overall increase in total land precipitation, intensified droughts remain prevalent in several regions (Supplementary Fig. 8a). Regions with reduced drought severity are those that have experienced increased precipitation during RS compared to MAX, consistently accompanied by a rise in heavy precipitation events (Fig. 4a and Supplementary Fig. 8a). In contrast, in N_E, although regions with increased precipitation also show a reduction in droughts (Supplementary Figs. 6a and 8b), these increases are not universally associated with elevated heavy precipitation (Fig. 4b). This indicates that the negative emissions lead to the alleviation of either heavy precipitation or drought in most regions, except for the Sahara and Northern Europe.

The changes in heavy precipitation and drought following the negative emissions are closely linked to precipitation changes driven by physiological effects, such as increased leaf area and enhanced evapotranspiration. The expansion of leaf area improves water capture and storage, thereby increasing water availability (i.e., increase in water storage) (Supplementary Table 1). Simultaneously, increased evapotranspiration continuously supplies water vapor into the atmosphere, leading to more frequent precipitation events, evidenced by the increase in the number and area of wet days (Fig. 4d and Supplementary Fig. 9) and the total amount of precipitation (Fig. 1b). This increase in precipitation frequency potentially contributes to a reduction in extreme precipitation and droughts occurrences by distributing rainfall more evenly, thereby enhancing the efficiency of water resources. This underscores the importance of negative emissions strategies in reducing potential future climate impacts and highlights the necessity of incorporating these strategies into climate projections and developing effective mitigation and adaptation strategies.

Discussion

Our results suggest that even if future measures achieve zero or negative CO_2 emissions, land precipitation will not return to current levels but will exceed those projected during the periods of highest CO_2 concentrations. Particularly under a negative emissions scenario, there is a notable overshoot in land precipitation. While this overshoot is driven by the delayed response of the climate system, it is further amplified by the transpiration changes from terrestrial vegetation. As CO_2 levels are restored, transpiration recovers from the suppression induced by high CO_2 concentrations, allowing transpiration to enhance precipitation. This mechanism leads to a further increase in land precipitation under the negative emissions scenario, despite relatively low temperatures compared to the zero emissions scenario. Our findings demonstrate that the land precipitation response under negative emissions is distinct from that under positive emissions, with vegetation playing an important role in the precipitation increase.

This study advances our understanding of precipitation responses to CO_2 removal by highlighting two key distinctions from previous work. First, most earlier studies have used concentration-driven CO_2 scenarios focused on temperature and precipitation hysteresis[25,28], without accounting for CO_2 outgassing from land and ocean as concentrations decline. In contrast, our emissions-driven experiment includes a fully interactive carbon cycle, capturing this outgassing and providing a more realistic representation of physiological feedback. Second, while previous studies emphasized reduced transpiration due to stomatal closure under positive CO_2 emissions[54], our results reveal the role of physiological processes in driving precipitation changes under the negative emissions scenario. These findings underscore the importance of vegetation in shaping hydrological outcomes under extended mitigation scenarios and highlight the value of emissions-based experiments in capturing long-term Earth system feedbacks.

Our findings further indicate substantial regional implications. While future climate impacts may worsen even after achieving zero emissions, substantial negative emissions could effectively mitigate several climate conditions, including hydrological extremes. Reductions in heavy precipitation are most significant in densely populated regions such as Eastern North America, South America, Central Africa, and Asia. Additionally, droughts are expected to decrease in Europe, Central America, and Western Asia. These regional patterns differ significantly from zero and negative emission scenarios, highlighting that the extreme events are not simply proportional to total precipitation.

This study has several limitations. First, it relies on the results from a single model. Although nine ensemble experiments were conducted for each scenario over a 400-year integration period, inter-model comparisons were not performed. Second, the experimental pathways used are highly idealized. The CO_2 concentration was increased to nearly twice the present-day levels, representing an idealized scenario designed to investigate long-term Earth system feedbacks. While this framework provides theoretical insight, it limits the direct applicability of the results to near-term climate policy. This underscores the need for complementary experiments based on more realistic mitigation pathways, such as achieving zero or negative emissions by 2050. Third, the focus of this study is on total terrestrial precipitation rather than regional variations. Additionally, detailed dynamical analyses of extreme events are not provided. While extreme events could be influenced by moisture flux convergence in some regions, such as Eastern North America, North-Eastern South America, Western and Central Europe, Western Africa, South Eastern Africa, and East Asia (Supplementary Fig. 6b), this aspect lies beyond the scope of this study. Fourth, the changes in precipitation observed under the negative emissions scenario are similar to those from the 1pctCO2-rad simulation in the C4MIP experiments[55]. However, these findings highlight the importance of CO_2 physiological effects, which could be crucial to understanding the reversibility of Earth systems.

Vegetation feedbacks remain a complex and regionally variable mechanism in shaping hydrological responses. Elevated CO_2 typically reduces stomatal conductance and evapotranspiration by increasing plant water use efficiency[52], while simultaneously enhancing LAI via CO_2 fertilization[56]. The net impact on evapotranspiration remains uncertain, as it depends on the relative strength of these opposing processes, which varies across climate conditions and vegetation types[38,57,58]. Some studies suggest the existence of a physiological threshold beyond which LAI-driven increases in transpiration can outweigh stomatal limitations and reverse the direction of evapotranspiration change[38,59]. These discrepancies underscore the need to better constrain the contributions of LAI versus stomatal closure in land surface models to improve future projections of the hydrological cycle.

This study highlights the critical role of physiological feedback in enhancing terrestrial precipitation under a negative emissions scenario, demonstrating its potential to improve the hydrological cycle and reduce the severity of extreme precipitation events. These findings underscore the need to move beyond net-zero targets toward negative emissions strategies—an increasingly important consideration for future climate policy. While current mitigation efforts often prioritize addressing immediate climate impacts, our findings suggest that early and sustained action can also deliver substantial long-term benefits for Earth system sustainability. This underlines the importance of forward-looking, comprehensive research to inform and guide effective climate response strategies.

Methods

Model configuration

The Community Earth System Model 2 (CESM2) was utilized to conduct an idealized CO_2 emission-driven simulation. This model is composed of physical components, including atmosphere, ocean, land, and cryosphere, which are fully integrated with the land and ocean carbon cycles[60]. The atmospheric model is the Community Atmosphere Model version 6 (CAM6), featuring a horizontal resolution of ~1° with 32 vertical levels. The ocean and sea ice models are the Parallel Ocean Program version 2 (POP2)[61] and the Community Ice CodE version 5 (CICE5)[62], respectively. The ocean components used a nominal ~1° horizontal resolution (meridional resolution ~0.27° near the equator) with 60 vertical levels. The Community Land Model Version 5 (CLM5)[46] has the same horizontal resolution as the atmosphere model. It characterizes the carbon and hydrological cycles of the land in CESM2, which has experienced significant advancements through the incorporation of new and updated processes and parameterizations. Notable enhancements include an accurate representation of historical cumulative CO_2 uptake and the seasonal cycle of net ecosystem production[46,63,64]. The ocean carbon cycles in CESM2 are depicted by the Marine Biogeochemistry Library (MARBL)[65].

CLM5 has been evaluated as part of an ensemble of simulations—including prescribed and prognostic vegetation states, multiple forcing datasets, and previous model versions (CLM4 and CLM4.5)—using the International Land Model Benchmarking (ILAMBv2) package[46]. It simulates LAI and evapotranspiration at a level comparable to the dataset and shows improved performance in capturing observed relationships between precipitation, LAI, and evapotranspiration. The CO_2 fertilization effect on LAI has been demonstrated in CLM5 through perturbed physics ensemble simulations[66] and historical single-forcing experiments[67]. In addition, under the SSP5-8.5 high-emission scenario, CLM5 simulates decreased stomatal conductance and evapotranspiration, along with increased LAI, consistent with expectations under elevated CO_2 concentrations[54]. These studies indicate that the model is capable of reasonably representing the relationship between vegetation and climate feedbacks.

Experimental design

To explore the impacts of different CO_2 emission trajectories, we designed idealized simulations based on both zero and negative emissions scenarios (Supplementary Fig. 1). In our model, anthropogenic CO_2 emissions increase linearly from 2000 to 2050, following the SSP5-8.5 scenario, with an annual increase of 1.09 GtCO2. After peaking in 2050, emissions decrease at the same rate until they reach zero by the year 2124. In the zero emissions scenario (Z_E), emissions remain at zero until the end of the simulation in 2400 (Supplementary Fig. 1a). In the negative emissions scenario (N_E), emissions continue to decrease at the same rate after reaching zero, until the global mean surface atmospheric CO_2 concentration returns to its initial value of approximately 383 ppm by the year 2197 (Supplementary Fig. 1b). Following this, CO_2 emissions are maintained at zero from 2197 until the end of simulation in 2400.

This simulation is driven by CO_2 emissions, where atmospheric CO_2 concentrations are determined not only by prescribed anthropogenic CO_2 emissions but also by CO2 fluxes from land and ocean, capturing changes in CO_2 concentration through carbon cycle-climate feedback. All non-CO_2 factors, such as land use and non-CO_2 greenhouse gas forcings, are held constant at the present-day (2000) levels. A total of nine ensemble members were conducted for each scenario, with slightly different initial conditions, initialized monthly from January to October (excluding September) in the year 2000, using the CESM2 esm-hist experiment.

To analyze the role of transpiration in land precipitation, an additional idealized experiment, referred to as the $N_{E\text{-}LAND}$ scenario, was conducted. The experiment utilized the same components as in the N_E, with initial conditions set to the year 2300, based on the first ensemble member. The atmospheric CO_2 concentration was fixed at 430 ppm—representative of conditions from 2300 to 2399—while the CO_2 concentration received by the land was fixed at 725 ppm, corresponding to the period of maximum CO_2 concentration (e.g., 2091 to 2120). This setup enables the quantification of CO_2-physiological forcing on land hydrology due to elevated CO_2 levels at the surface under similar climate conditions and allows for a comparison of the resulting changes in precipitation with those observed under a negative emission scenario. The experiment was carried out over 200 years, with the first 100 years used as a spin-up period and the subsequent 100 years analyzed.

Definition of indices

Atmospheric moisture budget. The atmospheric moisture budget can be expressed in the following form:

$$\frac{\partial w}{\partial t} = E - P - \int_{top}^{sfc} \nabla_p(\boldsymbol{u}q)\frac{dp}{g} \quad (1)$$

Where g is the gravitational acceleration, q is specific humidity, p is atmospheric pressure (*sfc* and *top* indicate the earth's surface and top of atmosphere, respectively), $\nabla_p()$ is the horizontal divergence in pressure coordinates, $\boldsymbol{u}$ is the horizontal wind vector, P is the precipitation rate, E is the evaporation rate, and $\frac{\partial w}{\partial t}$ is the tendency of total precipitable water. The last term of the right side is the total moisture flux convergence. A positive value is observed when atmospheric moisture is exported from the region. The change in total precipitable water is calculated as the difference between E minus P and moisture flux convergence.

Terrestrial water balance. The terrestrial water balance can be expressed as[68]:

$$\frac{dS_L}{dt} = P_L - E_L - R_L \quad (2)$$

Where $\frac{dS_L}{dt}$ represents the change in soil water storage, P_L is the land precipitation, E_L is the evapotranspiration, and R_L is the runoff.

Heavy precipitation index. The Expert Team on Climate Change Detection and Indices (ETCCDI) has well-defined a series of extreme precipitation indices. Generally, these indices can be classified into three main types: intensity, frequency, and duration. In this study, we selected the widely accepted and commonly used heavy precipitation index of maximum 1-day precipitation (Rx1day). The total fraction of areas with heavy precipitation is calculated as the percentage difference between the specific period and the reference period, divided by the reference period. This calculation is performed only for regions where the heavy precipitation index during the reference period exceeds 30 mm per day. Other indices, such as the number of days with precipitation greater than 30 mm (R30mm) and the maximum consecutive 5-day precipitation (Rx5day), are analyzed but are not presented as they show similar patterns to Rx1day. Eight ensemble members are used for each scenario to analyze the heavy precipitation index.

Drought index. The near-surface soil moisture deficit (drought) index is calculated using the total soil water content from 0 to 8 m depth.

Wet days index. The Wet days index, as used in the ETCCDI, is defined as the annual total of days with precipitation exceeding 1 mm. Eight ensemble members were utilized to analyze the index. The total fraction of areas with wet days is calculated as the percentage difference between the specific period and the reference period, divided by the reference period.

Area means. The Global mean values are calculated over the latitude range from 60° S to 90° N, excluding Antarctica. The land and ocean mean values are calculated by applying land and ocean masks, respectively.

Percentage change in precipitation. The percentage change in precipitation is calculated for each ensemble member relative to the reference period (2001–2030).

Significance test. The significance level was determined using a Kolmogorov–Smirnov two-sample test.

Regional acronyms. Using the regional domains defined in Figure SPM.3 of the Intergovernmental Panel on Climate Change Sixth Assessment Report Working Group I (IPCC AR6 WGI) Summary for Policymakers (SPM) report[69] (Supplementary Fig. 10), we calculated the area-averaged heavy precipitation (Fig. 4) and drought (Supplementary Fig. 8) for each region. These regions are represented by hexagons of equal size, positioned in their approximate geographical locations. The abbreviations used for each region are as follows:

North America: NWN (North-Western North America), NEN (North-Eastern North America), WNA (Western North America), CNA (Central North America), ENA (Eastern North America); Central America: NCA (Northern Central America), SCA (Southern Central America), CAR (Caribbean); South America: NWS (North-Western South America), NSA (Northern South America), NES (North-Eastern South America), SAM (South American Monsoon), SWS (South-Western South America), SES (South-Eastern South America), SSA (Southern South America); Europe: GIC (Greenland/Iceland), NEU (Northern Europe), WCE (Western and Central Europe), EEU (Eastern Europe), MED (Mediterranean); Africa: MED (Mediterranean), SAH (Sahara), WAF (Western Africa), CAF (Central Africa), NEAF (North Eastern Africa), SEAF (South Eastern Africa), WSAF (West Southern Africa), ESAF (East Southern Africa), MDG (Madagascar); Asia: RAR (Russian Arctic), WSB (West Siberia), ESB (East Siberia), RFE (Russian Far East), WCA (West Central Asia), ECA (East Central Asia), TIB (Tibetan Plateau), EAS (East Asia), ARP (Arabian Peninsula), SAS (South Asia), SEA (South East Asia); Australasia: NAU (Northern Australia), CAU (Central

Australia), EAU (Eastern Australia), SAU (Southern Australia), NZ (New Zealand); Ocean: ARO (Arctic Ocean), ARS (Arabian Sea), BOB (Bay of Bengal), EAO (Equatorial Atlantic Ocean), EIO (Equatorial Indic Ocean), EPO (Equatorial Pacific Ocean), NAO (N. Atlantic Ocean), NPO (N. Pacific Ocean), SAO (S. Atlantic Ocean), SIO (South Indic Ocean), SOO (Southern Ocean), SPO (S. Pacific Ocean), Small Islands: CAR (Caribbean).

Data availability

The CESM2 code is available at https://www.cesm.ucar.edu/models/cesm2/. The NCAR Command Language (NCL) is available at https://www.ncl.ucar.edu/. The data that support the findings of this study are available in Figshare with the identifier https://doi.org/10.6084/m9.figshare.30153862.v1[70]. Due to their large size, the raw CESM2 simulation outputs are available from the corresponding author upon request. Source data are provided at Figshare (https://doi.org/10.6084/m9.figshare.30153862.v1[70]).

Code availability

The code used in this study is available on Figshare (https://doi.org/10.6084/m9.figshare.30153862.v1[70]).

References

1. Friedlingstein, P. et al. Global carbon budget 2020. *Earth Syst. Sci. Data Discuss.* **2020**, 1–3 (2020).
2. Jones, C. D. et al. The zero emissions commitment model intercomparison project (ZECMIP) contribution to C4MIP: quantifying committed climate changes following zero carbon emissions. *Geosci. Model Dev.* **12**, 4375–4385 (2019).
3. Matthews, H. D. & Weaver, A. J. Committed climate warming. *Nat. Geosci.* **3**, 142–143 (2010).
4. Keller, D. P. et al. The carbon dioxide removal model intercomparison project (CDRMIP): rationale and experimental protocol for CMIP6. *Geosci. Model Dev.* **11**, 1133–1160 (2018).
5. Lawrence, M. G. et al. Evaluating climate geoengineering proposals in the context of the Paris Agreement temperature goals. *Nat. Commun.* **9**, 3734 (2018).
6. Swingedouw, D. et al. Early warning from space for a few key tipping points in physical, biological, and social-ecological systems. *Surv. Geophys.* **41**, 1237–1284 (2020).
7. Lenton, T. M. Early warning of climate tipping points. *Nat. Clim. change* **1**, 201–209 (2011).
8. Lenton, T. M. et al. Tipping elements in the Earth's climate system. *Proc. Natl. Acad. Sci. USA* **105**, 1786–1793 (2008).
9. Jeltsch-Thömmes, A., Stocker, T. F. & Joos, F. Hysteresis of the Earth system under positive and negative CO_2 emissions. *Environ. Res. Lett.* **15**, 124026 (2020).
10. Matthews, H. D. & Caldeira, K. Stabilizing climate requires near-zero emissions. *Geophys. Res. Lett.* https://doi.org/10.1029/2007GL032388 (2008).
11. An, S. I. et al. Global cooling hiatus driven by an AMOC overshoot in a carbon dioxide removal scenario. *Earth's. Future* **9**, e2021EF002165 (2021).
12. Oh, J. H., An, S. I., Shin, J. & Kug, J. S. Centennial memory of the Arctic Ocean for future Arctic climate recovery in response to a carbon dioxide removal. *Earth's. Future* **10**, e2022EF002804 (2022).
13. Wu, P., Jackson, L., Pardaens, A. & Schaller, N. Extended warming of the northern high latitudes due to an overshoot of the Atlantic meridional overturning circulation. *Geophys. Res. Lett.* https://doi.org/10.1029/2011GL049998 (2011).
14. Kug, J.-S. et al. Hysteresis of the intertropical convergence zone to CO_2 forcing. *Nat. Clim. Change* **12**, 47–53 (2022).
15. Oh, H. et al. Contrasting hysteresis behaviors of Northern Hemisphere land monsoon precipitation to CO2 pathways. *Earth's. Future* **10**, e2021EF002623 (2022).
16. Song, S.-Y. et al. Asymmetrical response of summer rainfall in East Asia to CO_2 forcing. *Sci. Bull.* **67**, 213–222 (2022).
17. Zickfeld, K., MacDougall, A. H. & Matthews, H. D. On the proportionality between global temperature change and cumulative CO_2 emissions during periods of net negative CO_2 emissions. *Environ. Res. Lett.* **11**, 055006 (2016).
18. Boucher, O. et al. Reversibility in an Earth System model in response to CO_2 concentration changes. *Environ. Res. Lett.* **7**, 024013 (2012).
19. Yang, Y.-M. et al. Fast reduction of Atlantic SST threatens Europe-wide gross primary productivity under positive and negative CO_2 emissions. *npj Clim. Atmos. Sci.* **7**, 117 (2024).
20. Hwang, J. et al. Asymmetric hysteresis response of mid-latitude storm tracks to CO_2 removal. *Nat. Clim. Change* **14**, 1–8 (2024).
21. Kim, S.-Y. et al. Hemispherically asymmetric Hadley cell response to CO_2 removal. *Sci. Adv.* **9**, eadg1801 (2023).
22. Mondal, S. K. et al. Hysteresis and irreversibility of global extreme precipitation to anthropogenic CO_2 emission. *Weather Clim. Extremes* **40**, 100561 (2023).
23. Jo, S. Y. et al. Hysteresis behaviors in East Asian extreme precipitation frequency to CO_2 pathway. *Geophys. Res. Lett.* **49**, e2022GL099814 (2022).
24. An, S.-I. et al. General circulation and global heat transport in a quadrupling CO_2 pulse experiment. *Sci. Rep.* **12**, 11569 (2022).
25. Kim, S.-K. et al. Widespread irreversible changes in surface temperature and precipitation in response to CO2 forcing. *Nat. Clim. Change* **12**, 834–840 (2022).
26. Wu, P., Wood, R., Ridley, J. & Lowe, J. Temporary acceleration of the hydrological cycle in response to a CO_2 rampdown. *Geophys. Res. Lett.* https://doi.org/10.1029/2010GL043730 (2010).
27. Cao, L., Bala, G. & Caldeira, K. Why is there a short-term increase in global precipitation in response to diminished CO_2 forcing? *Geophys. Res. Lett.* https://doi.org/10.1029/2011GL046713 (2011).
28. Yeh, S.-W., Song, S.-Y., Allan, R. P., An, S.-I. & Shin, J. Contrasting response of hydrological cycle over land and ocean to a changing CO_2 pathway. *npj Clim. Atmos. Sci.* **4**, 53 (2021).
29. Im, N. et al. Hysteresis of European summer precipitation under a symmetric CO_2 ramp-up and ramp-down pathway. *Environ. Res. Lett.* **19**, 074030 (2024).
30. Zhu, Z. et al. Greening of the Earth and its drivers. *Nat. Clim. change* **6**, 791–795 (2016).
31. Drake, B. G., Gonzàlez-Meler, M. A. & Long, S. P. More efficient plants: A consequence of rising atmospheric CO_2? *Annu. Rev. Plant Biol.* **48**, 609–639 (1997).
32. Ainsworth, E. A. & Long, S. P. What have we learned from 15 years of free-air CO2 enrichment (FACE)? A meta-analytic review of the responses of photosynthesis, canopy properties and plant production to rising CO_2. *N. Phytol.* **165**, 351–372 (2005).
33. Hong, T. et al. The response of vegetation to rising CO_2 concentrations plays an important role in future changes in the hydrological cycle. *Theor. Appl. Climatol.* **136**, 135–144 (2019).
34. Park, S.-W., Kim, J.-S. & Kug, J.-S. The intensification of Arctic warming as a result of CO2 physiological forcing. *Nat. Commun.* **11**, 2098 (2020).
35. Cao, L., Bala, G., Caldeira, K., Nemani, R. & Ban-Weiss, G. Importance of carbon dioxide physiological forcing to future climate change. *Proc. Natl. Acad. Sci. USA* **107**, 9513–9518 (2010).
36. Park, S.-W., Kug, J.-S., Jun, S.-Y., Jeong, S.-J. & Kim, J.-S. Role of cloud feedback in continental warming response to CO_2 physiological forcing. *J. Clim.* **34**, 8813–8828 (2021).
37. Skinner, C. B., Poulsen, C. J., Chadwick, R., Diffenbaugh, N. S. & Fiorella, R. P. The role of plant CO2 physiological forcing in shaping future daily-scale precipitation. *J. Clim.* **30**, 2319–2340 (2017).
38. Kooperman, G. J. et al. Forest response to rising CO_2 drives zonally asymmetric rainfall change over tropical land. *Nat. Clim. Change* **8**, 434–440 (2018).

39. Jeong, S.-J., Ho, C.-H., Park, T.-W., Kim, J. & Levis, S. Impact of vegetation feedback on the temperature and its diurnal range over the Northern Hemisphere during summer in a 2× CO_2 climate. *Clim. Dyn.* **37**, 821–833 (2011).
40. Dai, A. Recent climatology, variability, and trends in global surface humidity. *J. Clim.* **19**, 3589–3606 (2006).
41. Trenberth, K. E. et al. Observations. surface and atmospheric climate change. Chapter 3. (2007).
42. Park, S.-W. et al. How will global carbon cycle respond to negative emissions? *ESS Open Archive* (2023).
43. Wu, P., Ridley, J., Pardaens, A., Levine, R. & Lowe, J. The reversibility of CO_2 induced climate change. *Clim. Dyn.* **45**, 745–754 (2015).
44. Schwinger, J., Asaadi, A., Goris, N. & Lee, H. Possibility for strong northern hemisphere high-latitude cooling under negative emissions. *Nat. Commun.* **13**, 1095 (2022).
45. Oh, J.-H. et al. Emergent climate change patterns originating from deep ocean warming in climate mitigation scenarios. *Nat. Clim. Change* **14**, 1–7 (2024).
46. Lawrence, D. M. et al. The Community Land Model version 5: description of new features, benchmarking, and impact of forcing uncertainty. *J. Adv. Model. Earth Syst.* **11**, 4245–4287 (2019).
47. Sellers, P. J. et al. A revised land surface parameterization (SiB2) for atmospheric GCMs. Part I: model formulation. *J. Clim.* **9**, 676–705 (1996).
48. Zhang, J. et al. Insights into the molecular mechanisms of CO_2-mediated regulation of stomatal movements. *Curr. Biol.* **28**, R1356–R1363 (2018).
49. Keenan, T. F. et al. Increase in forest water-use efficiency as atmospheric carbon dioxide concentrations rise. *Nature* **499**, 324–327 (2013).
50. Medlyn, B. E. et al. Stomatal conductance of forest species after long-term exposure to elevated CO2 concentration: a synthesis. *N. Phytol.* **149**, 247–264 (2001).
51. Cox, P. M. et al. The impact of new land surface physics on the GCM simulation of climate and climate sensitivity. *Clim. Dyn.* **15**, 183–203 (1999).
52. Swann, A. L. S., Hoffman, F. M., Koven, C. D. & Randerson, J. T. Plant responses to increasing CO2 reduce estimates of climate impacts on drought severity. *Proc. Natl. Acad. Sci. USA* **113**, 10019–10024 (2016).
53. Donat, M. G., Lowry, A. L., Alexander, L. V., O'Gorman, P. A. & Maher, N. More extreme precipitation in the world's dry and wet regions. *Nat. Clim. Change* **6**, 508–513 (2016).
54. Yuan, T. et al. Potential decoupling of CO_2 and Hg uptake process by global vegetation in the 21st century. *Nat. Commun.* **15**, 4490 (2024).
55. Jones, C. D. et al. C4MIP–the coupled climate–carbon cycle model intercomparison project: experimental protocol for CMIP6. *Geosci. Model Dev.* **9**, 2853–2880 (2016).
56. Norby, R. J. & Zak, D. R. Ecological lessons from free-air CO_2 enrichment (FACE) experiments. *Ann. Rev. Ecol. Evol. Syst.* **42**, 181–203 (2011).
57. Fatichi, S. et al. Partitioning direct and indirect effects reveals the response of water-limited ecosystems to elevated CO2. *Proc. Natl. Acad. Sci. USA* **113**, 12757–12762 (2016).
58. Forzieri, G., Alkama, R., Miralles, D. G. & Cescatti, A. Satellites reveal contrasting responses of regional climate to the widespread greening of Earth. *Science* **356**, 1180–1184 (2017).
59. McDermid, S. S. et al. Disentangling the regional climate impacts of competing vegetation responses to elevated atmospheric CO_2. *J. Geophys. Res.***126**, e2020JD034108 (2021).
60. Danabasoglu, G. et al. The Community Earth System Model version 2 (CESM2). *J. Adv. Model. Earth Syst.* **12**, e2019MS001916 (2020).
61. Smith, R. et al. The parallel ocean program (POP) reference manual ocean component of the community climate system model (CCSM) and community earth system model (CESM). *LAUR-01853* **141**, 1–140 (2010).
62. Bailey, D. A., Holland, M. M., DuVivier, A. K., Hunke, E. C. & Turner, A. K. Impact of a new sea ice thermodynamic formulation in the CESM2 sea ice component. *J. Adv. Model. Earth Syst.* **12**, e2020MS002154 (2020).
63. Bonan, G. B. et al. Model structure and climate data uncertainty in historical simulations of the terrestrial carbon cycle (1850–2014). *Glob. Biogeochem. Cycles* **33**, 1310–1326 (2019).
64. Collier, N. et al. The international land model benchmarking (ILAMB) system: design, theory, and implementation. *J. Adv. Model. Earth Syst.* **10**, 2731–2754 (2018).
65. Long, M. C. et al. Simulations with the marine biogeochemistry library (MARBL). *J. Adv. Model. Earth Syst.* **13**, e2021MS002647 (2021).
66. Fisher, R. A. et al. Parametric controls on vegetation responses to biogeochemical forcing in the CLM5. *J. Adv. Model. Earth Syst.* **11**, 2879–2895 (2019).
67. Lombardozzi, D. L. et al. Agricultural fertilization significantly enhances amplitude of land-atmosphere CO_2 exchange. *Nat. Commun.* **16**, 1742 (2025).
68. Kleidon, A. & Schymanski, S. Thermodynamics and optimality of the water budget on land: a review. *Geophys. Res. Lett.* https://doi.org/10.1029/2008GL035393 (2008).
69. Masson-Delmotte, V. P. et al. IPCC, 2021: summary for policymakers. in: *Climate Change 2021: The Physical Science Basis. Contribution of Working Group I to the Sixth Assessment Report of the Intergovernmental Panel on Climate Change*. (IPCC, 2021).
70. Shin, J. Dataset for "Negative CO2 emissions to mitigate long-term extremes in land hydrological cycle". *figshare* https://doi.org/10.6084/m9.figshare.30153862.v1 (2025).

Acknowledgements

This work was supported by the National Research Foundation of Korea (NRF) grant funded by the Korea government (MSIT) (NRF-2022R1A3B1077622) and by Korea Environment Industry and Technology Institute(KEITI) through the Project for developing an observation-based GHG emissions geospatial information map, funded by Korea Ministry of Environment(MOE) (RS-2023-00232066). J.S. was supported by the Basic Science Research Program through the National Research Foundation of Korea (NRF), funded by the Ministry of Education (RS-2024-00413360), and the Woods Hole Oceanographic Institution (WHOI) Grow The Base Fund. The CESM simulation was conducted by H.-J.S. and was carried out on the supercomputer supported by the National Center for Meteorological Supercomputer of Korea Meteorological Administration (KMA), the National Supercomputing Center with supercomputing resources, associated technical support (KSC-2025-CHA-0001), and the Korea Research Environment Open NETwork (KREONET). Supplementary Fig. 1 was designed by K.N.

Author contributions

J. Shin and J.-S. Kug designed the study. J. Shin developed the code, prepared the figures, and wrote the initial draft of the manuscript. S.-I. An designed the carbon dioxide emission scenarios. S.-E. Park conducted the CESM2 ensemble simulations. J. Kam and C.-K. Park computed the drought index. S.-I. An, J. Kam, S.-W. Park, H. Oh, S.-W. Yeh, S. Jeong, and J.-S. Kim contributed to the interpretation of the data and the writing of the manuscript.

Competing interests

The authors declare no competing interests.

Additional information

Supplementary information The online version contains supplementary material available at https://doi.org/10.1038/s41467-026-70945-8.

Correspondence and requests for materials should be addressed to Jong-Seong Kug.

Peer review information *Nature Communications* thanks the anonymous reviewers for their contribution to the peer review of this work. A peer review file is available.

Reprints and permissions information is available at http://www.nature.com/reprints

Publisher's note Springer Nature remains neutral with regard to jurisdictional claims in published maps and institutional affiliations.

Open Access This article is licensed under a Creative Commons Attribution-NonCommercial-NoDerivatives 4.0 International License, which permits any non-commercial use, sharing, distribution and reproduction in any medium or format, as long as you give appropriate credit to the original author(s) and the source, provide a link to the Creative Commons licence, and indicate if you modified the licensed material. You do not have permission under this licence to share adapted material derived from this article or parts of it. The images or other third party material in this article are included in the article's Creative Commons licence, unless indicated otherwise in a credit line to the material. If material is not included in the article's Creative Commons licence and your intended use is not permitted by statutory regulation or exceeds the permitted use, you will need to obtain permission directly from the copyright holder. To view a copy of this licence, visit http://creativecommons.org/licenses/by-nc-nd/4.0/.

© The Author(s) 2026